Environmental Science & Technology

pubs.acs.org/est

Article

Biomass-Derived Provenance Dominates Glacial Surface Organic Carbon in the Western Himalaya

Sarwar Nizam,* Indra S. Sen, Velu Vinoj, Valier Galy, David Selby, Mohammad F. Azam, Satyendra K. Pandey, Robert A. Creaser, Avinash K. Agarwal, Akhilendra P. Singh, and Michael Bizimis

Cite This: *Environ. Sci. Technol.* 2020, 54, 8612–8621

Read Online

ACCESS | Metrics & More | Article Recommendations | Supporting Information

ABSTRACT: The origin, transport pathway, and spatial variability of total organic carbon (OC) in the western Himalayan glaciers are poorly understood compared to those of black carbon (BC) and dust, but it is critically important to evaluate the climatic role of OC in the region. By applying the distribution of OC activation energy; ^{14}C activity; and radiogenic isotopes of $^{208}Pb/^{204}Pb$, $^{207}Pb/^{204}Pb$, and $^{206}Pb/^{204}Pb$ in glacial debris and atmospheric particulate matter (PM_{10} size fraction), we demonstrate that 98.3 ± 1.6 and 1.7 ± 1.6% of OC in western Himalayan glaciers are derived from biomass and petrogenic sources, respectively. The $\delta^{13}C$ and N/C composition indicates that the biomass is a complex mixture of C3 vegetation and autochthonous photoautotrophic input modified by heterotrophic microbial activity. The data set reveals that the studied western Himalayan glacier has negligible contributions from fossil-fuel-derived particles, which contrasts to the central and eastern Himalayan glaciers that have significant contributions from fossil fuel sources. We show that this spatial variability of OC sources relates to regional differences in air mass transport pathways and precipitation regimes over the Himalaya. Moreover, our observation suggests that biomass-derived carbon could be the only primary driver of carbon-induced glacier melting in the western Himalaya.

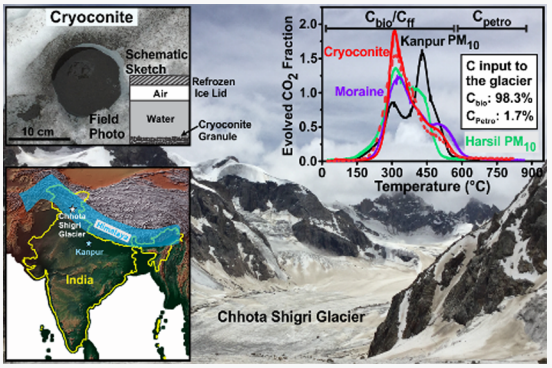

1. INTRODUCTION

Worldwide, glaciers are losing mass at an average rate of 0.48 ± 0.20 m water equivalent per year (m w.e. yr^{-1}),[1] with the rate of Himalayan glacier mass wastage nearly doubling (−0.43 ± 0.14 m w.e. yr^{-1}) in recent years.[2] This accelerated mass loss is considered to be primarily related to the well-established long-term increase of the earth's near-surface temperature and anthropogenic climate change.[3,4] In addition to this warming, the reduction of surface ice albedo by ice surface deposits of dark-colored impurities constitutes an additional control of the glacier melting rate.[5−7] Impurities that darken the ice surface, directly increase the heat absorption, and thus enhance ice melting comprise dust, black carbon (BC, e.g., soot), and other forms of organic carbon (OC) derived from combustion sources.[8−11] In this study, OC refers to the total organic carbon that comprises the entire pool of organic carbon including both organic and elemental carbon. Further, we classify the OC as OC_{ff} (fossil fuel) and OC_{bio} (biomass) referring to OC derived from, respectively, fossil fuel and biomass sources, such as biomass burning derived particles, atmospheric organic matters, and glacial microbes.[5]

The contribution to glacier surface darkening of particulate matter and its attendant impact on glacial melt across high Asian mountain glaciers varies. For example, the main contributor to glacier surface warming in the eastern Himalaya and central Asia is BC, while mineral dust is a dominant factor in the western Himalaya.[12] As a result, previous studies have mainly focused on BC and dust, owing to their higher heat absorption capacities.[13−16] Therefore, limited research on total OC has led to substantial uncertainties and incomplete knowledge of the impact of OC on the Himalaya and Tibetan Plateau.[17−19] Thus, given the almost 20% albedo reduction related to OC for glaciers in Asia,[12] a thorough assessment of the origin, transport pathways, and spatial distribution of OC is paramount to reduce the uncertainties in estimating the impact of carbon on the rate of glacial melting of Himalayan glaciers. In addition to the albedo effect of light-absorbing impurities,[20,21] carbonaceous aerosols also warm up the air mass over glaciers and support microbial life,[20−22] both of which further contribute to an enhanced rate of glacier melting. It is also worth noting that algal or microbial communities on the glacier surface act as a sink for carbon and other impurities and may yield a greater positive feedback on glacier melting when

Received: April 29, 2020
Revised: June 25, 2020
Accepted: June 25, 2020
Published: June 25, 2020

https://dx.doi.org/10.1021/acs.est.0c02710
Environ. Sci. Technol. 2020, 54, 8612–8621

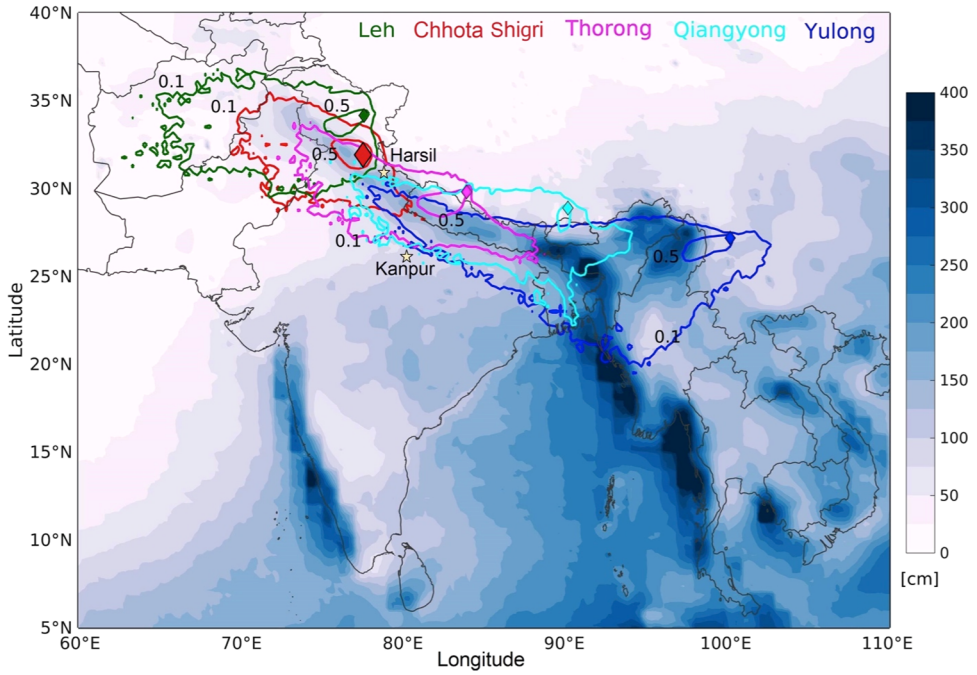

Figure 1. Climatological rainfall (TRMM_3B42_v7) with overlain trajectory density plot for a few glaciers in the Himalayan−Tibetan Plateau region. The line contours represent the fractional number of trajectories passing through a particular grid of spatial resolution (0.25 × 0.25°). For clarity, only two contours (of values 0.5 and 0.1) are shown for each receptor site. Here, 168 h HYSPLIT back trajectories starting from each of the five-receptor site for every hour (24 × 365) of the year 2016 were used. Thorong, Qiangyong, and Yulong sites have ∼50% fossil-fuel-derived carbon.[25] Stars represent the aerosol sampling location, and the highlighted large polygon is our glacier sampling site. The figure shows that there is a marked difference between the rainfall amounts between the western and eastern Himalayan glacier sites with eastern Himalaya receiving higher rainfall. The 0.5 and 0.1 contour intervals show that the western Himalayan glacier sites are mostly influenced by air mass from western parts of the Himalaya, whereas central and eastern Himalayan glaciers are impacted by air mass from the Indo-Gangetic Plain (IGP), which is characterized by a high level of anthropogenic activities (Figure S1). Seasonal trajectory density plots further show that wind trajectory origin is near similar irrespective of the seasons, with most trajectories originating over a small region around the studied glacier (Figure S2).

compared to OC_{ff}..[23] As such, constraints on the composition of OC will help better quantify the future impact of increasing anthropogenic emission on surrounding Himalayan glaciers (Figure S1) and its attendant control on the hydrological regimes of glacier-sourced large river systems such as the Indus, Ganges, and Brahmaputra. The findings will also aid in quantifying the contribution of Himalayan glacier melt to eustatic sea-level rise,[1] currently estimated to raise the sea level by 0.52 cm by the end of 21st century.[24]

In contrast to model-based approaches,[26−28] recent radiocarbon measurements of BC particles deposited on glaciers and in aerosols revealed a much higher (∼50%) fossil fuel contribution across the Himalayan−Tibetan Plateau.[25] These radiocarbon measurements were however restricted to the central and eastern Himalayan regions, which fall under the strong influence of the Indian summer monsoon. Further, the eastern and western areas of the Himalayan region have different climatology, hydrology, meteorology, as well as glacier behavior and dynamics.[29−31] The large geographical spread (∼2500 km) of the Himalaya over different climate regimes makes it very difficult to extend the findings of one climate regime to the other. Moreover, in situ OC measurements of glacier and snow samples in the western Himalaya including the Hindu Kush and Karakoram regions are not available, despite the fact that the western region holds >70% of the total ice mass of the Himalaya.[32] With one-sixth of the world's population dependent on the Himalayan glacier meltwater and an increase in anthropogenic emissions in the Indian subcontinent (Figure S1), understanding the origin and transport pathways of OC on the western Himalayan glaciers and its impact on the glacier melting rate is an issue of global significance.

To understand the origin, transport pathway, and spatial variability of OC on the western Himalayan glaciers, this study focuses on the source area and origin of dust and OC on the ablation zone (>4500 m a.s.l.) of the Chhota Shigri Glacier (CSG, 32.2° N, 77.5° E) in the Lahaul-Spiti valley of the western Himalaya, India (Figure 1). Cryoconite and supraglacial moraine sediments from the CSG surface were investigated to characterize the origin of carbonaceous particles. Cryoconites are small-water-filled depressions containing a dark-colored mixture of dust, OC, BC, and microbes collected over several years. Further, to constrain the source end members, atmospheric particulate matter (PM_{10}) were collected from Harsil (31.1 °N, 78.7 °E, 2634 m a.s.l.) and Kanpur (26.1° N, 80.2° E). The Harsil site is located in a high-altitude remote Himalayan forested area that records a history of major forest fires (Figure S3). Harsil is >125 km from major urban settlements and industrial activities; thus, the collected aerosol at Harsil serves as the best proxy for OC_{bio} and pristine Himalayan end member. To obtain the best estimate of OC_{ff} aerosol, a sample was collected from ∼5 km north of a coal-fired thermal power plant (Panki Thermal Power Plant) and 1 km west of a National Highway (NH91) in Kanpur—one of the largest industrialized centers in the Indo-Gangetic Plain (Figure 1). Analysis of samples followed a multidisciplinary approach, coupling organic and inorganic geochemical tracers including ramped pyrolysis oxidation (RPO), ^{14}C activity,

https://dx.doi.org/10.1021/acs.est.0c02710
Environ. Sci. Technol. 2020, 54, 8612−8621

Table 1. RPO Analysis Results for Cryoconite (C9 and C14), Moraine (DF6), and Aerosol Samples[a,b]

	T (°C)		m_F	E_a (1σ)	F_m (2σ)	$\delta^{13}C$	^{14}C age
sample RPO fraction	min	max	μg C	(kJ mol^{-1})	(fraction modern)	(‰)	(cal yr BP)
C9-F1	150	300	100.3	138 ± 6	1.0191 ± 0.0020	−20.57	>modern
C9-F2	300	326	106.6	140 ± 4	1.0408 ± 0.0021	−18.37	>modern
C9-F3	326	361	112.1	146 ± 7	1.0399 ± 0.0020	−18.07	>modern
C9-F4	361	412	102.5	157 ± 8	1.0126 ± 0.0026	−18.77	>modern
C9-F5	412	480	90.3	171 ± 9	0.9822 ± 0.0019	−20.03	145 ± 15
C9-F6	480	794	88.0	191 ± 13	0.7947 ± 0.0021	−21.00	1850 ± 20
C14-F1	150	318	136.4	136 ± 7	1.0563 ± 0.0021	−24.93	>modern
C14-F2	318	375	135.0	148 ± 6	1.0529 ± 0.0021	−22.99	>modern
C14-F3	375	465	135.0	165 ± 9	1.0137 ± 0.0023	−23.58	>modern
C14-F4	465	560	100.0	188 ± 8	0.788 ± 0.0018	−25.1	1910 ± 20
C14-F5	560	850	36.8	208 ± 14	0.4609 ± 0.0039	−27.17	6220 ± 70
DF6-F1	150	298	108.0	132 ± 8	1.0461 ± 0.0022	−10.76	>modern
DF6-F2	298	336	100.1	142 ± 6	1.0485 ± 0.0025	−22.43	>modern
DF6-F3	336	387	109.0	153 ± 8	1.0063 ± 0.0023	−22.28	>modern
DF6-F4	387	483	100.6	168 ± 10	0.9688 ± 0.0020	−23.17	255 ± 15
DF6-F5	483	784	57.6	193 ± 15	0.6068 ± 0.0020	−24.71	4010 ± 30
KA-F1	125	306	104.1	130 ± 11	0.8155 ± 0.0019	−27.66	1640 ± 20
KA-F2	306	377	100.3	147 ± 10	0.7982 ± 0.0018	−26.17	1810 ± 20
KA-F3	377	425	103.1	166 ± 6	0.6182 ± 0.0018	−25.11	3860 ± 25
KA-F4	425	462	102.0	171 ± 6	0.5237 ± 0.0022	−24.60	5200 ± 35
KA-F5	462	655	101.4	183 ± 8	0.4179 ± 0.0017	−24.91	7010 ± 30
HA-F1	125	293	53.6	127 ± 11	0.9884 ± 0.0030	−26.83	95 ± 25
HA-F2	293	335	51.9	142 ± 6	1.0096 ± 0.0036	−26.23	>modern
HA-F3	335	385	52.8	152 ± 7	1.0029 ± 0.0033	−24.78	>modern
HA-F4	385	439	52.1	165 ± 6	0.9775 ± 0.0033	−23.23	180 ± 25
HA-F5	439	605	34.0	175 ± 7	0.9364 ± 0.0039	−22.13	530 ± 35

[a]KA, Kanpur aerosol. [b]HA, Harsil aerosol. m_F indicates the mass of carbon (as CO_2) contained in RPO fraction F.

$\delta^{13}C$, $^{208}Pb/^{204}Pb$, $^{207}Pb/^{204}Pb$, $^{206}Pb/^{204}Pb$, TOC, N, and heavy metal concentrations with hybrid single-particle Lagrangian integrated trajectory (HYSPLIT), an air mass trajectory model, to determine the OC origin and identify transport pathways.

2. MATERIALS AND METHODS

2.1. Sampling Details. Cryoconite debris was collected from 20 sites in the ablation zone (4515−4928 m a.s.l.) of the CSG during July, 2017. In addition to cryoconite, five moraine debris samples were also collected. The samples were first dried on a hot plate at ∼70 °C to remove the moisture content. Moraine debris samples were sieved to obtain bulk (DB < 3 mm) and particulate (<63 μm, DF) fractions for geochemical analysis. Bulk cryoconite and moraine debris samples (DB and DF) were ground to a homogeneous powder (20 μm size) in an agate mill for further chemical analysis. Atmospheric particulate matter (PM_{10} size fraction) sampling in Kanpur and Harsil was carried out using high-volume (1000 L/min) atmospheric aerosol samplers (Envirotech PM_{10} sampler, model APM 460 DXNL). In Kanpur and Harsil, the PM_{10} sampler was operated for 24 (on January 1, 2016) and 48 h (April 12−14, 2016), respectively. The detailed sampling protocol description is outlined in the work of Nizam and Sen.[33]

2.2. Ramped Pyrolysis Oxidation (RPO), ^{14}C Age, Bulk $\delta^{13}C$, N, and C Analyses. The RPO analysis was carried out at the National Ocean Sciences Accelerator Mass Spectrometer (NOSAMS, Woods Hole Oceanographic Institution) facility. The RPO instrument involves continuous sample heating, with CO_2 evolved being trapped for dual C-isotope analysis. Importantly, RPO analyzes 100% of OC in the sample, irrespective of the nature of OC. Two cryoconite (C9 and C14), one moraine (DF6), and two aerosol samples were selected for RPO analysis. The instrumental makeup and analytical protocol adopted for RPO analysis have been described in detail in previous studies.[34,35] Briefly, powder sample aliquots of 30−70 mg were loaded into a precombusted (at 850 °C for 5 h) quartz reactor, heated at a 5 °C min $^{-1}$ ramp rate in a two-stage oven. This incremental heating leads to the release of CO_2, which was cryogenically purified, trapped, and flame-sealed into a glass tube containing nuggets of Ag (∼10 mg) and CuO (∼100 mg). The CO_2 concentration in the carrier gas (in parts per million by volume, ppm CO_2) is continuously measured at a resolution of 1 s using an infrared gas analyzer. CO_2 collected at user-defined temperature intervals is referred to as RPO fractions. Each RPO fraction collected is graphitized with the radiocarbon abundance determined via accelerated mass spectrometry at NOSAMS and reported as fraction modern (F_m). Meanwhile, a 10% split of each RPO fraction was used for stable isotope ($\delta^{13}C$) analysis using a dual-inlet isotope ratio mass spectrometer (IRMS).

The $\delta^{13}C$ values are expressed in parts per mill (‰) notation relative to Vienna Pee Dee Belemnite (VPDB). The F_m and $\delta^{13}C$ ratios of the RPO fractions are reported in Table 1. In addition, bulk $\delta^{13}C$, total organic carbon (OC), and total nitrogen (N) were also measured in all of the cryoconite and selected moraine samples using IRMS at Woods Hole Oceanographic Institution (Table S1). The bulk $\delta^{13}C$ value calculated as the mass-weighted average of all RPO fractions showed a good agreement with the measured bulk $\delta^{13}C$ value,

https://dx.doi.org/10.1021/acs.est.0c02710
Environ. Sci. Technol. 2020, 54, 8612−8621

Table 2. Radiogenic Lead Isotope Composition of Selected Cryoconite (Cx) and Moraine (DF) Samples[a]

sample id	$^{208}Pb/^{204}Pb$	2SE	$^{207}Pb/^{204}Pb$	2SE	$^{206}Pb/^{204}Pb$	2SE	$^{207}Pb/^{206}Pb$	2SE
C1	38.91787	0.00546	15.70946	0.00182	18.78705	0.00159	0.83616	0.00003
C3	39.13549	0.00684	15.73477	0.00250	18.80094	0.00244	0.83691	0.00004
C5	39.23825	0.00680	15.74825	0.00218	19.02939	0.00224	0.82757	0.00005
C9	38.67497	0.00868	15.67102	0.00286	18.65789	0.00250	0.83991	0.00005
C11	38.67167	0.00520	15.68224	0.00166	18.55690	0.00178	0.84508	0.00003
C13	38.58314	0.00728	15.68314	0.00250	18.50767	0.00242	0.84740	0.00004
C14	38.38955	0.00552	15.65890	0.00204	18.32318	0.00202	0.85456	0.00003
C17	38.40762	0.00426	15.66683	0.00146	18.35741	0.00139	0.85343	0.00003
C18	38.40409	0.00630	15.65812	0.00242	18.30283	0.00202	0.85551	0.00004
C19	38.21132	0.00476	15.63569	0.00164	18.15303	0.00163	0.86133	0.00003
DF6	38.42784	0.00562	15.68993	0.00208	18.40597	0.00196	0.85239	0.00005
DF12	39.74669	0.00720	15.76498	0.00246	19.32824	0.00226	0.81567	0.00003

[a]Note: Total Pb concentration in blank = 0.2 ± 0.16 ppb (1 SD, n = 4), reproducibility uncertainty level = 1σ.

with the exception of moraine sample DF6. The mismatch appears to be driven by the high $\delta^{13}C$ value of the first RPO fraction collected for this sample. We inferred that this enriched stable isotope composition is related to some technical error during IRMS analysis. The results for all of the RPO (and IRMS) analyses were blank, and kinetic isotope fractionation was corrected.[36] Corrected data was used to calculate the activation energy distribution using the rampedpyrox Python package,[37] which has been described in detail in previous studies.[35] Radiocarbon age (in ^{14}C yr BP) was calculated using corrected F_m values and the Libby half-life as age = $-8033 \ln(F_m)$.

2.3. Lead Isotope Analysis. Ten cryoconite and two moraine samples (DF) were selected for Pb isotope analysis. The Pb isotopic data was obtained from the Radiogenic Isotope Facility of the Department of Earth and Atmospheric Sciences at the University of Alberta. Approximately 4−12 mg of sample powder (depending on lead abundance) was dissolved in ultrapure HF/HNO_3 at 100 °C for 2 days. Sample solutions were then evaporated under ULPA-filtered air and converted to chlorides using 6N HCl and then to bromides using 2N HBr. Pb was purified by standard anion exchange chromatography using HBr and HCl as eluents under ULPA-filtered conditions. The isotopic composition of Pb was then measured by Nu Plasma MC-ICPMS in static analysis mode. The measured Pb isotope ratios were corrected for instrumental mass bias using the agreed value for the $^{203}Tl/^{205}Tl$ ratio measured simultaneously with each Pb analysis.[38] Overall reproducibility of any Pb isotope measurement is based on >6 years of analyses of the SRM981 Pb isotope standard. At the first uncertainty level, the reproducibility of the SRM981-measured isotopic ratios are $^{206}Pb/^{204}Pb$ = 0.016%, $^{207}Pb/^{204}Pb$ = 0.018%, and $^{208}Pb/^{204}Pb$ = 0.018%. The most widely accepted values for this Pb isotope standard are those determined by double-spiked TIMS analysis in a previous study,[39] which are $^{206}Pb/^{204}Pb$ = 16.936, $^{207}Pb/^{204}Pb$ = 15.489, and $^{208}Pb/^{204}Pb$ = 36.701. The absolute values of Pb isotope ratios for SRM981 determined during the course of the analyses reported here are $^{206}Pb/^{204}Pb$ = 16.936, $^{207}Pb/^{204}Pb$ = 15.488, and $^{208}Pb/^{204}Pb$ = 36.690. The Pb isotope ratios are reported in Table 2.

2.4. Heavy Metal Analysis. Heavy metal concentration analyses were performed at the Indian Institute of Technology Kanpur using a quadrupole inductively coupled plasma mass spectrometer (Thermo Fisher Scientific, Q-ICP-MS) system. Briefly, approximately 25 mg of sample powder was digested using a mixture of HF (three parts) and HNO_3 (one part). Six procedural blanks and a reference material SBC-1 (shale) from the US Geological Survey (USGS) were also digested following the same procedures. The final concentrations were blank-corrected using the average procedural blank concentrations, and the matrix effect was corrected by in normalization (Table S1). Average blank corrections were less than 1% for most of the elements. The measured Sc, V, Cr, Ni, Cu, Zn, and Pb concentrations of SBC-1 were 20 ± 1, 205 ± 3, 101 ± 2, 81 ± 1, 30 ± 0.2, 191 ± 2, and 33 ± 1 (1 SD, n = 6), respectively, which is in close agreement with the USGS certified values of 20 ± 0.2, 220 ± 1.4, 109 ± 1, 83 ± 0.8, 31 ± 0.6, 186 ± 2, and 35 ± 0.3, respectively.

2.5. Air Mass Back Trajectory Analysis. The hybrid single-particle Lagrangian integrated trajectory (HYSPLIT) model was used to compute the air parcel back trajectories for every hour for five different sites including Leh, Chhota Shigri, Thorong, Qiangyong, and Yulong for the year 2016 (Figure 1). The archived meteorological analysis from the Global Data Assimilation System (GDAS) model of the National Centers for Environmental Prediction (NCEP) was used to estimate the trajectories. Annual as well as seasonal trajectory analysis was carried out to elucidate the major source regions of air mass reaching the Himalaya (Figures 1 and S2). A total of 24 × 365 or 8760 trajectory pairs were simulated for each site. A density map was created at a resolution of 0.25 × 0.25° to obtain fraction of total trajectories passing through each of the grid cells. This provided an indication of the percentage or probability of influence of each grid point to the air mass reaching the receptor site. Two contour intervals of 0.1 and 0.5 that represented 10 and 50% trajectories passing through any grid were created for each site.

3. RESULTS AND DISCUSSION

The distribution of OC activation energy (E_a), $\delta^{13}C$, and ^{14}C content (expressed as fraction modern, F_m) for cryoconite, moraine sediments (particulate fraction), and PM_{10} were compared to fingerprint the sources of OC (Figure 2). Activation energy is a proxy for OC reactivity, and each OC pool has a distinct E_a distribution reflecting its overall bonding environment (e.g., molecular composition, association with mineral surfaces).[35] Using E_a, $\delta^{13}C$, and ^{14}C ages, it is thus possible to fingerprint the sources of OC. For example, biomass-derived OC have lower E_a (<150 kJ mol^{-1}), high F_m

https://dx.doi.org/10.1021/acs.est.0c02710
Environ. Sci. Technol. 2020, 54, 8612−8621

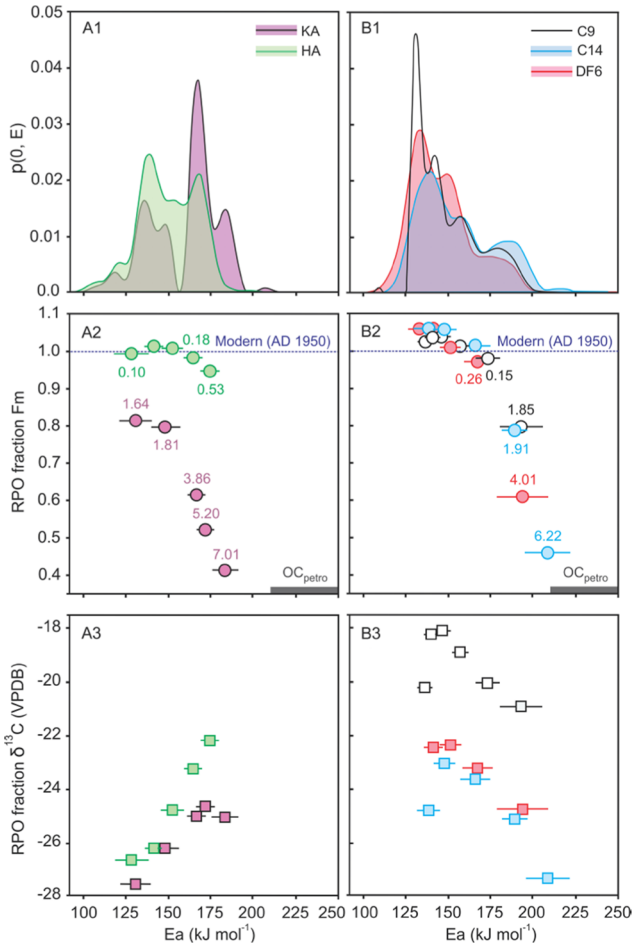

Figure 2. Apportionment of OC sources from RPO analysis. OC activation energy (E_a) distributions (p (0, E) of (A1) aerosol (Kanpur aerosol, KA; Harsil aerosol, HA) and (B1) glacier samples (cryoconite, C9 and C14; moraine fine fraction, DF6). Radiocarbon (F_m in fraction) composition of each RPO fraction of the samples with the associated radiocarbon age (in cal kyr BP) and stable carbon ($\delta^{13}C$ in ‰) are plotted in middle (A2 and B2) and lower (A3 and B3) panels, respectively. Peak reactivity at ca. 165 kJ mol^{-1} and the associated low F_m value and old ^{14}C ages highlight OC_{ff} contributions in KA. Low OC thermal recalcitrance (peak < 150 kJ mol^{-1}) and associated high F_m values and modern ages comparable to OC_{bio} and HA reflect recently fixed sources. OC in glacier samples contains small contributions of high E_a material reflecting binary mixing between a dilute petrogenic end member and a more concentrated biomass/biospheric end member. Dashed lines in both the middle panels represent modern radiocarbon age.

(~1.0), and modern ages, whereas fossil-derived OC possess higher E_a (>150 kJ mol^{-1}) and F_m = 0.[40] Among the fossil sources, OC derived from Himalayan petrogenic sources (OC_{petro}) has a much higher E_a (≥200 kJ mol^{-1}) than fossil-fuel-derived OC (OC_{ff} < 200 kJ mol^{-1}).[40,41]

PM_{10} collected from Harsil and Kanpur have distinct E_a distributions and ^{14}C compositions (Table 1 and Figure 2). The E_a distributions of Harsil and Kanpur PM_{10} OC show a predominant peaks at ca. 135 and 165 kJ mol^{-1}, respectively. Harsil PM_{10} OC is also characterized by young ^{14}C ages (RPO F_m values >0.94, bulk F_m = 0.99). A predominant E_a peak at ca. 135 kJ mol^{-1} and young ^{14}C ages of Harsil PM_{10} OC clearly correspond to OC_{bio}.[40] It is possible that some of the particles could contain soil organic carbon (SOC). However, SOC is expected to be preaged, as observed in mineral soils globally and suspended sediments of Himalayan-sourced rivers.[42,43] Further, dust contributions from arid areas (e.g., Thar Desert) would similarly be expected to carry an old ^{14}C signature owing to conditions promoting organic matter preservation. Our data is not consistent with SOC inputs as it shows a flat, near-modern ^{14}C age across the E_a spectrum. In contrast, Kanpur PM_{10} OC is characterized by lower F_m values (0.4 < F_m < 0.8, bulk F_m = 0.64) and corresponding older ^{14}C ages. A predominant E_a peak at ca. 165 kJ mol^{-1} and older ^{14}C ages of Kanpur PM_{10} OC reveal significant contributions from a fossil fuel source. The lower E_a peak in Kanpur PM_{10} OC (ca. 135 kJ mol^{-1}) also points toward some OC_{bio} contribution. A simple binary mixing calculation revealed that Kanpur PM_{10} OC is composed of ca. 36% of OC_{ff} and 64% of OC_{bio}. The PM_{10} RPO data further suggest that OC_{bio} and OC_{ff} have overlapping E_a distributions, although OC_{ff} is more heavily concentrated at higher E_a values.

OC in cryoconite and moraine sediment have similar E_a distributions with peak reactivity between ca. 125 and 150 kJ mol^{-1}. The low E_a and high F_m values and modern ^{14}C ages support that OC in these RPO fractions is derived from recently fixed OC sources (OC_{bio}, F_m ~ 1, modern age) such as biomass burning, autochthonous photoautotrophic biomass, and heterotrophic microorganisms. Overall, the E_a and ^{14}C signature of cryoconite and moraine sediments are similar to those of Harsil PM_{10}, confirming an overwhelmingly dominant OC_{bio} input to both cryoconite and moraine sediments. A small portion of cryoconite and moraine OC is characterized by high E_a (>180 kJ mol^{-1}) and low F_m (older ^{14}C ages) values. The presence of aged OC exclusively at high E_a values however precludes OC_{ff} as a source because Kanpur PM_{10} RPO data show that OC_{ff} is distributed over the entire E_a spectrum. Instead, we argue that the high E_a RPO fractions contain a mixture of biomass and petrogenic (rock-derived, OC_{petro}) OC. Indeed, OC_{petro} has been shown to be characterized by high E_a (i.e., >200 kJ mol^{-1}) and F_m values equal to 0.[40] A mass balance approach assuming a binary mixing of ^{14}C-dead OC and biomass-derived OC with a ^{14}C age equal to that of Harsil PM_{10}, shows that 1.7 ± 1.6% of OC in cryoconite and moraine sediments is derived from ^{14}C-dead sources. This proportion translates into a C concentration of 0.02 ± 0.02%. Such a low concentration of ^{14}C-dead OC is consistent with the expected OC_{petro} concentration in the high-grade crystalline rocks of the CSG catchment and Himalayan rocks in general.[44] It is also lower than the average OC content of bulk moraine samples (0.064 ± 0.020%), which, based on bulk geochemical characterization, are dominated by OC_{petro}. We conclude that cryoconite and moraine sediments have negligible OC_{ff} and a mixture of OC_{bio} (98.3 ± 1.6%) and minor OC_{petro} (1.7 ± 1.6%) inputs.

Additionally, we used stable carbon isotopes ($\delta^{13}C$) to further establish the source of OC_{bio} in the cryoconite and moraine sediments. The majority of the cryoconite samples have a distinct $\delta^{13}C$ composition with respect to the surrounding moraine sediments, as well as to cryoconite samples from Greenland and the Arctic.[45,46] The $\delta^{13}C$ in cryoconite samples ranges between −24.9 and −18.2‰ (average −21.8 ± 1.7‰, n = 20, 1 SD), which is higher than that for moraine sediments (−22.5 to −26.7‰, average −24.2 ± 1.3‰, n = 10, 1 SD). In general, carbonaceous aerosol derived from burnt C3-type biomass sources in the Indian subcontinent should have a $\delta^{13}C$ value of ca. −26‰,[47]

https://dx.doi.org/10.1021/acs.est.0c02710
Environ. Sci. Technol. 2020, 54, 8612−8621

which can exhibit a maximum fractionation up to 0.5‰ due to the burning emission effect.[49] Burning-induced ^{13}C fractionation of C3-type vegetation is therefore insufficient to explain the observed $\delta^{13}C$ enrichment in cryoconite. Therefore, it can be postulated that cryoconite draws some of its enriched $\delta^{13}C$ signature from additional sources or processes.

The $\delta^{13}C$ enrichment in cryoconite samples can be best explained by contributions from photoautotrophic and heterotrophic microorganisms in supraglacial cryoconite that produce enrichment of N and $\delta^{13}C$ values.[22,46] Biomass humification processes can also produce enriched $\delta^{13}C$ values, but the RPO-^{14}C data are incompatible with significant SOC inputs. The N/C vs $\delta^{13}C$ plot (Figure 3A) suggests that

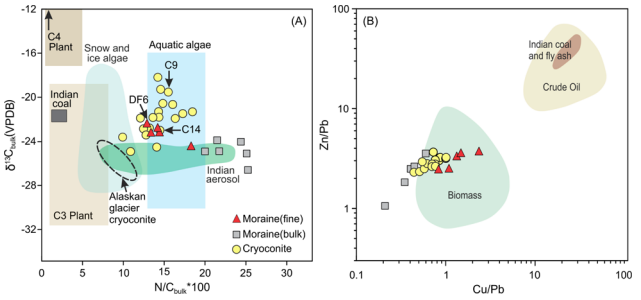

Figure 3. OC source inference from stable C isotopes and N/C and heavy metal ratios. (A) Bulk organic N/C and $\delta^{13}C$ mixing diagram showing the composition of cryoconite and moraine samples compared to that of tentative end members. Nitrogen and ^{13}C enrichment in cryoconite compared to that in bulk moraine suggests mixing between ^{13}C-poor, N-poor OM characteristic of biomass and ^{13}C-rich, N-rich OM typical of algae/microbes dwelling on the glacier surface. Linear mixing trend between fine and bulk moraine suggests mixing between petrogenic and biospheric inputs. Literature references: C3 plant, C4 plant, and aquatic algae;[58] snow and ice algae,[22,59,60] Alaskan glacier cryoconite.[45] Indian coal and aerosol.[47] (B) Heavy metal ratios in glacier samples compared to those in biomass,[48] Indian coal and fly ash,[61] and crude oil.[62]

cryoconite samples are composed of a mixture of ^{13}C-depleted and N-poor organic matter that could correspond to primary C3-derived OC, with ^{13}C-enriched and N-rich organic matter that reflects microbial communities growing in the snow/ice environment. According to the RPO data, the ^{13}C-rich, N-rich component is also enriched in ^{14}C (i.e., it has been fixed recently) and relatively labile, further suggesting that it corresponds to microbial biomass and/or algae. However, finer apportionment of the different sources of biospheric OC in cryoconite samples would require compound-specific biomarker data. To summarize, our data suggest that the OC in cryoconite and moraine sediments is a complex mixture of C3-type biomass and autochthonous photoautotrophic inputs modified by heterotrophic microbial activity. An overall biomass source signature is also supported by heavy metal ratios (Zn/Pb vs Cu/Pb; Figure 3B), assuming that the metal ratios retained the source signature during transportation and transformation changes.

In addition to carbon systematics and heavy metal concentrations, $^{206}Pb/^{204}Pb$ and $^{208}Pb/^{204}Pb$ were used as additional independent tracers to identify the residues of fossil fuel signature on the CSG. The radiogenic Pb isotopes (Table 2) as well as heavy metal enrichment factor (Figure S4) also support the absence of fossil fuel signature in cryoconite and moraine sediments from the CSG. Moreover, $^{206}Pb/^{204}Pb$ and

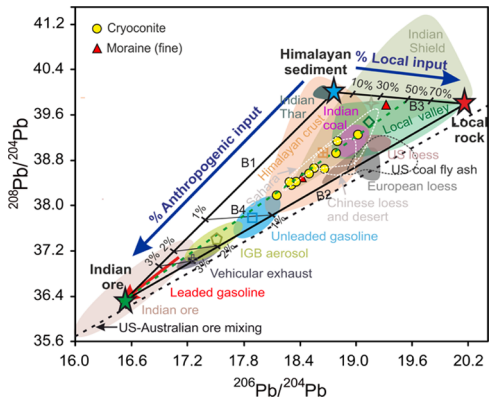

Figure 4. Mixing arrays in $^{206}Pb^{204}Pb$ versus $^{208}Pb^{204}$ isotopic space. The yellow circles and red triangles are new data points; literature data shown with colored fields and open symbols within the field denote their average compositions. Thick black, dashed green, and dashed black lines are two-component mixing lines. The color-filled stars denote end member compositions used in mixing calculations. Curves B1 and B2 define mixing of Indian ore with Himalayan sediment (HS) and local crust (LC), respectively, while B3 represents mixing between LC and HS composition. Curves B4 is a mixing line between Indian ores with a sediment mixture comprising of 50% HS and 50% LC. We selected HS ($^{206}Pb/^{204}Pb$ = 18.81, $^{208}Pb/^{204}Pb$ = 39.99, Pb = 26.7 ppm)[63] and LC ($^{206}Pb^{204}Pb$ = 20.15, $^{208}Pb^{204}Pb$ = 39.79, Pb = 33 ppm)[64] as a natural source end member. As an anthropogenic source end member representative, Indian ore ($^{206}Pb/^{204}Pb$ = 16.42, $^{208}Pb/^{204}Pb$ = 37.27, Pb = 4000 ppm)[65,66] was chosen with the view that Pb used in various anthropogenic activities mined from these ores inherits its source signature. Literature references for other regional source end members are Indian shield,[67] Indian coal,[68] US coal fly ash,[69] IGB aerosol,[70−73] Sahara,[74,75] European loess,[76] Chinese loess and desert,[77−79] Thar,[77] US loess,[79] unleaded gasoline,[80] vehicular exhaust,[81] leaded gasoline,[82,83] and US-Australian ore.[84]

$^{208}Pb/^{204}Pb$ overlap with that of the Himalayan crust (Figure 4). The highly linear correlation between $^{206}Pb/^{204}Pb$ and $^{208}Pb/^{204}Pb$ further implies that these elements are sourced from two dominant end members. Mixing calculations using the Pb isotope systematically show a negligible anthropogenic contribution (<1%, Figure 4). The triple lead isotope data ($^{207}Pb/^{206}Pb$ versus $^{208}Pb/^{206}Pb$) also supports the absence of anthropogenic pollutant contribution in the studied glacier site (Figure S5). Our results differ from previous findings that the Himalayan glaciers in general receive significant long-range transported dust from Africa, the Middle East, and the Thar Desert, as well as from the Indo-Gangetic Plain, India.[50,51]

The OC activation energy distribution; ^{14}C, $\delta^{13}C$, $^{208}Pb/^{204}Pb$, $^{207}Pb/^{204}Pb$, and $^{206}Pb/^{204}Pb$; and TOC, N, and heavy metal concentrations, therefore, suggest that the studied western Himalayan glaciers have a negligible contribution from OC derived from fossil fuel combustion sources. The difference between our findings and a previous study reporting ~50% fossil-fuel-sourced carbon contribution in central and eastern Himalayan glaciers[25] can be explained by the air mass transport pathway and rainfall intensity. HYSPLIT air mass trajectory modeling results reveal that the eastern and central Himalayan glaciers that have received up to half of the BC from fossil fuel sources draw a significant fraction of their air

https://dx.doi.org/10.1021/acs.est.0c02710
Environ. Sci. Technol. 2020, 54, 8612−8621

mass from the heavily polluted Indo-Gangetic Plain (IGP) (Figure 1). In contrast, annual and seasonal (Figures 1 and S2) air mass back trajectory modeling at the study site shows that the western Himalayan region receives limited air mass transport from the polluted IGP and less rainfall as compared to the central and eastern Himalayan regions, confirming the limited transport of ambient anthropogenic pollutants from the IGP.

The estimated glacial mass loss rates between 2000 and 2016 in western, central, and eastern Himalaya are similar (−0.40, −0.35, and −0.53 m w.e yr^{-1}, respectively).[52] The glacial mass loss rate reported for CSG (−0.56 m w.e. yr^{-1} between 2002 and 2014)[53] is slightly higher than regional averages. Since glacial mass loss is similar across the Himalaya and CSG is essentially free from OC_{ff}, our observation suggests that OC_{bio} would be the primary driver of carbon-induced glacier melting in the western Himalaya. Direct aerosol measurement studies on the western and northwestern Himalaya hill stations also support a predominant burnt carbon biomass source.[54,55] Given that it is well known that OC_{ff} particles are more readily transported over long distances compared to OC_{bio},[56] and thus if OC_{bio} are transported from geographically distant sources, OC_{ff} particles are expected to be similar or higher in concentration compared to OC_{bio} in western Himalayan glaciers. The near absence of OC_{ff} and prevalence of local air mass circulation therefore indicate that carbonaceous particles in the western Himalaya are only derived from locally burnt biomass sources. Thus, given that OC emissions are projected to be 21−28 Tg by 2050,[57] leading to new climate policies to curb global carbon emissions in urban centers, considering that the impact of local carbonaceous aerosols on glacier mass loss in the western Himalaya is necessary to model the change in the glacial mass of western Himalayan glaciers.

■ ASSOCIATED CONTENT

Supporting Information

The Supporting Information is available free of charge at https://pubs.acs.org/doi/10.1021/acs.est.0c02710.

Difference in carbonaceous aerosol emissions; trajectory density plot; annual mean climatology of fire counts; average enrichment factor for heavy metals; triple isotope plot of Pb for glacier samples; and total organic carbon, total nitrogen, bulk stable carbon, and heavy metal concentration in cryoconite and moraine samples (PDF)

(PDF)

■ AUTHOR INFORMATION

Corresponding Author

Sarwar Nizam − *Department of Earth Sciences, Indian Institute of Technology Kanpur, Kanpur, Uttar Pradesh 208016, India;* orcid.org/0000-0002-6589-723X; Email: sarwar@iitk.ac.in

Authors

Indra S. Sen − *Department of Earth Sciences, Indian Institute of Technology Kanpur, Kanpur, Uttar Pradesh 208016, India;* orcid.org/0000-0001-7302-2313

Velu Vinoj − *School of Earth, Ocean and Climate Sciences, Indian Institute of Technology Bhubaneswar, Bhubaneswar, Odisha 752050, India;* orcid.org/0000-0001-8573-6073

Valier Galy − *Department of Marine Chemistry and Geochemistry, Woods Hole Oceanographic Institution (WHOI), Woods Hole, Massachusetts 02543, United States*

David Selby − *Department of Earth Sciences, University of Durham, Durham DH1 3LE, U.K.; State Key Laboratory of Geological Processes and Mineral Resources, School of Earth Resources, China University of Geosciences, Wuhan 430074, China*

Mohammad F. Azam − *Discipline of Civil Engineering, Indian Institute of Technology Indore, Indore 453552, India*

Satyendra K. Pandey − *School of Earth, Ocean and Climate Sciences, Indian Institute of Technology Bhubaneswar, Bhubaneswar, Odisha 752050, India*

Robert A. Creaser − *Department of Earth & Atmospheric Sciences University of Alberta, Edmonton, Alberta, Canada T6G2R3*

Avinash K. Agarwal − *Engine Research Laboratory, Department of Mechanical Engineering, Indian Institute of Technology, Kanpur, Uttar Pradesh 208016, India;* orcid.org/0000-0002-7777-785X

Akhilendra P. Singh − *Engine Research Laboratory, Department of Mechanical Engineering, Indian Institute of Technology, Kanpur, Uttar Pradesh 208016, India*

Michael Bizimis − *School of Earth, Ocean and Environment, University of South Carolina, Columbia, South Carolina 29208, United States*

Complete contact information is available at: https://pubs.acs.org/10.1021/acs.est.0c02710

Author Contributions

I.S.S. conceived the study. S.N. and M.F.A did the fieldwork. S.N. performed laboratory measurements. S.N., I.S.S., V.V., and S.K.P. developed the air mass back trajectory models. S.N., I.S.S., V.G., V.V., A.K.A., A.K.S., and D.S. analyzed the data. R.A.C. and M.B. contributed to radiogenic isotope analysis and discussions. S.N. and I.S.S. wrote the paper with input from all authors.

Notes

The authors declare no competing financial interest.

■ ACKNOWLEDGMENTS

This work was supported by the Department of Science and Technology, Government of India, Climate Change Program (SPLICE) (Grant DST/CCP/Aerosol/86/2017(C)) and the Science & Engineering Research Board (SERB) (Grant EMR/2015/000439) to I.S.S. S.N. is thankful for the IIT-Kanpur Ph.D. scholarship. We thank the Indian Institute of Technology Kanpur (IIT-Kanpur), National Ocean Sciences Accelerator Mass Spectrometer (NOSAMS) Facility, Woods Hole Oceanographic Institution (WHOI), and Durham University for providing access to instrumentation and support. D.S. acknowledges the Total Endowment Fund and the Dida Scholarship of CUG, Wuhan. M.F.A. acknowledges the INSPIRE Faculty Grant from DST-INPSIRE, Government of India. We thank four anonymous reviewers for their constructive comments that helped to improve this contribution.

■ REFERENCES

(1) Zemp, M.; Huss, M.; Thibert, E.; Eckert, N.; McNabb, R.; Huber, J.; Barandun, M.; Machguth, H.; Nussbaumer, S. U.; Gärtner-Roer, I.; Thomson, L.; Paul, F.; Maussion, F.; Kutuzov, S.; Cogley, J.

G. Global Glacier Mass Changes and Their Contributions to Sea-Level Rise from 1961 to 2016. *Nature* **2019**, *568*, 382−386.
(2) Maurer, J. M.; Schaefer, J. M.; Rupper, S.; Corley, A. Acceleration of Ice Loss across the Himalayas over the Past 40 Years. *Sci. Adv.* **2019**, *5*, No. eaav7266.
(3) Lau, W. K. M.; Kim, M. K.; Kim, K. M.; Lee, W. S. Enhanced Surface Warming and Accelerated Snow Melt in the Himalayas and Tibetan Plateau Induced by Absorbing Aerosols. *Environ. Res. Lett.* **2010**, *5*, No. 025204.
(4) Prasad, A. K.; S. Yang, K. H.; El-Askary, H. M.; Kafatos, M. Melting of Major Glaciers in the Western Himalayas: Evidence of Climatic Changes from Long Term MSU Derived Tropospheric Temperature Trend (1979-2008). *Ann. Geophys.* **2009**, *27*, 4505−4519.
(5) Santra, S.; Verma, S.; Fujita, K.; Chakraborty, I.; Boucher, O.; Takemura, T.; Burkhart, J. F.; Matt, F.; Sharma, M. Simulations of Black Carbon (BC) Aerosol Impact over Hindu Kush Himalayan Sites: Validation, Sources, and Implications on Glacier Runoff. *Atmos. Chem. Phys.* **2019**, *19*, 2441−2460.
(6) Ming, J.; Wang, Y.; Du, Z.; Zhang, T.; Guo, W.; Xiao, C.; Xu, X.; Ding, M.; Zhang, D.; Yang, W. Widespread Albedo Decreasing and Induced Melting of Himalayan Snow and Ice in the Early 21st Century. *PLoS One* **2015**, *10*, No. e0126235.
(7) Xu, Y.; Ramanathan, V.; Washington, W. M. Observed High-Altitude Warming and Snow Cover Retreat over Tibet and the Himalayas Enhanced by Black Carbon Aerosols. *Atmos. Chem. Phys. Discuss.* **2015**, *15*, 19079−19109.
(8) Skiles, S. M. K.; Painter, T. Daily Evolution in Dust and Black Carbon Content, Snow Grain Size, and Snow Albedo during Snowmelt, Rocky Mountains, Colorado. *J. Glaciol.* **2017**, *63*, 118−132.
(9) He, C.; Liou, K. N.; Takano, Y.; Chen, F.; Barlage, M. Enhanced Snow Absorption and Albedo Reduction by Dust-Snow Internal Mixing: Modeling and Parameterization. *J. Adv. Model. Earth Syst.* **2019**, *11*, 3755−3776.
(10) Kuchiki, K.; Aoki, T.; Niwano, M.; Matoba, S.; Kodama, Y.; Adachi, K. Elemental Carbon, Organic Carbon, and Dust Concentrations in Snow Measured with Thermal Optical and Gravimetric Methods: Variations during the 2007−2013 Winters at Sapporo, Japan. *J. Geophys. Res.: Atmos.* **2015**, *120*, 868−882.
(11) Zhang, Y.; Kang, S.; Gao, T.; Schmale, J.; Liu, Y.; Zhang, W.; Guo, J.; Du, W.; Hu, Z.; Cui, X.; Sillanpää, M. Dissolved Organic Carbon in Snow Cover of the Chinese Altai Mountains, Central Asia: Concentrations, Sources and Light-Absorption Properties. *Sci. Total Environ.* **2019**, *647*, 1385−1397.
(12) Yasunari, T. J.; Koster, R. D.; Lau, W. K. M.; Kim, K. Impact of Snow Darkening via Dust, Black Carbon, and Organic Carbon on Boreal Spring Climate in the Earth System. *J. Geophys. Res.: Atmos.* **2015**, *120*, 5485−5503.
(13) He, C.; Flanner, M. G.; Chen, F.; Barlage, M.; Liou, K. N.; Kang, S.; Ming, J.; Qian, Y. Black Carbon-Induced Snow Albedo Reduction over the Tibetan Plateau: Uncertainties from Snow Grain Shape and Aerosol-Snow Mixing State Based on an Updated SNICAR Model. *Atmos. Chem. Phys.* **2018**, *18*, 11507−11527.
(14) Ming, J.; Cachier, H.; Xiao, C.; Qin, D.; Kang, S.; Hou, S.; Xu, J. Black Carbon Record Based on a Shallow Himalayan Ice Core and Its Climatic Implications. *Atmos. Chem. Phys.* **2008**, *8*, 1343−1352.
(15) Schmale, J.; Flanner, M.; Kang, S.; Sprenger, M.; Zhang, Q.; Guo, J.; Li, Y.; Schwikowski, M.; Farinotti, D. Modulation of Snow Reflectance and Snowmelt from Central Asian Glaciers by Anthropogenic Black Carbon. *Sci. Rep.* **2017**, *7*, No. 40501.
(16) Kaspari, S.; Painter, T. H.; Gysel, M.; Skiles, S. M.; Schwikowski, M. Seasonal and Elevational Variations of Black Carbon and Dust in Snow and Ice in the Solu-Khumbu, Nepal and Estimated Radiative Forcings. *Atmos. Chem. Phys.* **2014**, *14*, 8089−8103.
(17) Yan, F.; He, C.; Kang, S.; Chen, P.; Hu, Z.; Han, X.; Gautam, S.; Yan, C.; Zheng, M.; Sillanpää, M.; Raymond, P. A.; Li, C. Deposition of Organic and Black Carbon: Direct Measurements at Three Remote Stations in the Himalayas and Tibetan Plateau. *J. Geophys. Res.: Atmos.* **2019**, *124*, 9702−9715.
(18) Xu, B.; Yao, T.; Liu, X.; Wang, N. Elemental and Organic Carbon Measurements with a Two-Step Heating-Gas Chromatography System in Snow Samples from the Tibetan Plateau. *Ann. Glaciol.* **2006**, *43*, 257−262.
(19) Chen, M.; Zeng, C.; Zhang, F.; Kang, S.; Li, C. Characteristics of Dissolved Organic Matter from a Transboundary Himalayan Watershed: Relationships with Land Use, Elevation, and Hydrology. *ACS Earth Space Chem.* **2020**, *4*, 449−456.
(20) Zhang, Y.; Kang, S.; Cong, Z.; Schmale, J.; Sprenger, M.; Li, C.; Yang, W.; Gao, T.; Sillanpaa, M.; Li, X.; Liu, Y.; Chen, P.; Zhang, X. Light-absorbing impurities enhance glacier albedo reduction in the southeastern Tibetan plateau. *J. Geophys. Res.* **2017**, *122*, 6915−6933.
(21) Ji, Z.; Kang, S.; Cong, Z.; Zhang, Q.; Yao, T. Simulation of Carbonaceous Aerosols over the Third Pole and Adjacent Regions: Distribution, Transportation, Deposition, and Climatic Effects. *Clim. Dyn.* **2015**, *45*, 2831−2846.
(22) Hamilton, T. L.; Havig, J. Primary Productivity of Snow Algae Communities on Stratovolcanoes of the Pacific Northwest. *Geobiology* **2017**, *15*, 280−295.
(23) Stibal, M.; Box, J. E.; Cameron, K. A.; Langen, P. L.; Yallop, M. L.; Mottram, R. H.; Khan, A. L.; Molotch, N. P.; Chrismas, N. A. M.; Quaglia, F. C.; Remias, D.; Smeets, C. J. P. P.; Broeke, M. R.; van den. Ryan, J. C.; Hubbard, A.; Tranter, M.; As, D.; van. Ahlstrøm, A. P. Algae Drive Enhanced Darkening of Bare Ice on the Greenland Ice Sheet. *Geophys. Res. Lett.* **2017**, *44*, 463−471.
(24) Giesen, R. H.; Oerlemans, J. Climate-Model Induced Differences in the 21st Century Global and Regional Glacier Contributions to Sea-Level Rise. *Clim. Dyn.* **2013**, *41*, 3283−3300.
(25) Li, C.; Bosch, C.; Kang, S.; Andersson, A.; Chen, P.; Zhang, Q.; Cong, Z.; Chen, B.; Qin, D.; Gustafsson, Ö. Sources of Black Carbon to the Himalayan-Tibetan Plateau Glaciers. *Nat. Commun.* **2016**, *7*, No. 12574.
(26) Soni, A.; Decesari, S.; Shridhar, V.; Prabhu, V.; Panwar, P.; Marinoni, A. Investigation of Potential Source Regions of Atmospheric Black Carbon in the Data Deficit Region of the Western Himalayas and Its Foothills. *Atmos. Pollut. Res.* **2019**, *10*, 1832−1842.
(27) Alvarado, M. J.; Winijkul, E.; Adams-Selin, R.; Hunt, E.; Brodowski, C.; Lonsdale, C. R.; Shindell, D. T.; Faluvegi, G.; Kleiman, G.; Mosier, T. M.; Kumar, R. Sources of Black Carbon Deposition to the Himalayan Glaciers in Current and Future Climates. *J. Geophys. Res.: Atmos.* **2018**, *123*, 7482−7505.
(28) Kopacz, M.; Mauzerall, D. L.; Wang, J.; Leibensperger, E. M.; Henze, D. K.; Singh, K. Origin and Radiative Forcing of Black Carbon Transported to the Himalayas and Tibetan Plateau. *Atmos. Chem. Phys.* **2011**, *11*, 2837−2852.
(29) Kapnick, S. B.; Delworth, T. L.; Ashfaq, M.; Malyshev, S.; Milly, P. C. D. Snowfall Less Sensitive to Warming in Karakoram than in Himalayas Due to a Unique Seasonal Cycle. *Nat. Geosci.* **2014**, *7*, 834−840.
(30) Lutz, A. F.; Immerzeel, W. W.; Shrestha, A. B.; Bierkens, M. F. P. Consistent Increase in High Asia's Runoff Due to Increasing Glacier Melt and Precipitation. *Nat. Clim. Change* **2014**, *4*, 587−592.
(31) Maussion, F.; Scherer, D.; Mölg, T.; Collier, E.; Curio, J.; Finkelnburg, R. Precipitation Seasonality and Variability over the Tibetan Plateau as Resolved by the High Asia Reanalysis. *J. Clim.* **2014**, *27*, 1910−1927.
(32) Frey, H.; Machguth, H.; Huss, M.; Huggel, C.; Bajracharya, S.; Bolch, T.; Kulkarni, A.; Linsbauer, A.; Salzmann, N.; Stoffel, M. Estimating the Volume of Glaciers in the Himalayan-Karakoram Region Using Different Methods. *Cryosphere* **2014**, *8*, 2313−2333.
(33) Nizam, S.; Sen, I. S. Effect of Southwest Monsoon Withdrawal on Mass Loading and Chemical Characteristics of Aerosols in an Urban City over the Indo-Gangetic Basin. *ACS Earth Space Chem.* **2018**, *2*, 347−355.
(34) Rosenheim, B. E.; Day, M. B.; Domack, E.; Schrum, H.; Benthien, A.; Hayes, J. M. Antarctic Sediment Chronology by

https://dx.doi.org/10.1021/acs.est.0c02710
Environ. Sci. Technol. 2020, 54, 8612−8621

Programmed-Temperature Pyrolysis: Methodology and Data Treatment. Geochemistry. *Geophys. Geosyst.* **2008**, *9*, 1−16.
(35) Hemingway, J. D.; Rothman, D. H.; Rosengard, S. Z.; Galy, V. V. Technical Note: An Inverse Method to Relate Organic Carbon Reactivity to Isotope Composition from Serial Oxidation. *Biogeosciences* **2017**, *14*, 5099−5114.
(36) Hemingway, J. D.; Galy, V. V.; Gagnon, A. R.; Grant, K. E.; Rosengard, S. Z.; Soulet, G.; Zigah, P. K.; McNichol, A. P. Assessing the Blank Carbon Contribution, Isotope Mass Balance, and Kinetic Isotope Fractionation of the Ramped Pyrolysis/Oxidation Instrument at Nosams. *Radiocarbon* **2017**, *59*, 179−193.
(37) Hemingway, J. D. Rampedpyrox: Open-Source Tools for Thermoanalytical Data Analysis, 2016. Http://Pypi.Python.Org/Pypi/Rampedpyrox. (accessed June 25, 2019).
(38) Belshaw, N.; Freedman, P.; O'Nions, R.; Frank, M.; Guo, Y. A New Variable Dispersion Double-Focusing Plasma Mass Spectrometer with Performance Illustrated for Pb Isotopes. *Int. J. Mass Spectrom.* **1998**, *181*, 51−58.
(39) Todt, W.; Cliff, R. A.; Hanser, A.; Hofmann, A. W. *Evaluation of a 202 Pb- 205 Pb Double Spike for High-Precision Lead Isotope Analysis. In Earth Processes: Reading the Isotopic Code*; Basu, A. S. H., Ed.; Blackwell Publishing Limited: AGU, Washington, D.C., 1995; Vol. *95*, pp 429−437.
(40) Hemingway, J. D.; Hilton, R. G.; Hovius, N.; Eglinton, T. I.; Haghipour, N.; Wacker, L.; Chen, M. C.; Galy, V. V. Microbial Oxidation of Lithospheric Organic Carbon in Rapidly Eroding Tropical Mountain Soils. *Science* **2018**, *360*, 209−212.
(41) Pendergraft, M. A.; Rosenheim, B. E. Varying Relative Degradation Rates of Oil in Different Forms and Environments Revealed by Ramped Pyrolysis. *Environ. Sci. Technol.* **2014**, *48*, 10966−10974.
(42) Galy, V.; Eglinton, T. Protracted Storage of Biospheric Carbon in the Ganges-Brahmaputra Basin. *Nat. Geosci.* **2011**, *4*, 843−847.
(43) French, K. L.; Hein, C. J.; Haghipour, N.; Wacker, L.; Kudrass, H. R.; Eglinton, T. I.; Millennial, V. G. Soil Retention of Terrestrial Organic Matter Deposited in the BengalFan. *Sci. Rep.* **2018**, *8*, No. 11997.
(44) Galy, V.; France-Lanord, C.; Beyssac, O.; Faure, P.; Kudrass, H.; Palhol, F. Efficient Organic Carbon Burial in the Bengal Fan Sustained by the Himalayan Erosional System. *Nature* **2007**, *450*, 407−410.
(45) McCrimmon, D. O.; Bizimis, M.; Holland, A.; Ziolkowski, L. A. Supraglacial Microbes Use Young Carbon and Not Aged Cryoconite Carbon. *Org. Geochem.* **2018**, *118*, 63−72.
(46) Musilova, M.; Tranter, M.; Bennett, S. A.; Wadham, J.; Anesio, A. M. Stable Microbial Community Composition on the Greenland Ice Sheet. *Front. Microbiol.* **2015**, *6*, 1−10.
(47) Agnihotri, R.; Mandal, T. K.; Karapurkar, S. G.; Naja, M.; Gadi, R.; Ahammmed, Y. N.; Kumar, A.; Saud, T.; Saxena, M. Stable Carbon and Nitrogen Isotopic Composition of Bulk Aerosols over India and Northern Indian Ocean. *Atmos. Environ.* **2011**, *45*, 2828−2835.
(48) Cuiping, L.; Chuangzhi, W.; Yanyongjie; Haitao, H. Chemical elemental characteristics of biomass fuels in China. *Biomass Bioenergy* **2004**, *27* (2), 119−130.
(49) Turekian, V. C.; MacKo, S.; Ballentine, D.; Swap, R. J.; Garstang, M. Causes of Bulk Carbon and Nitrogen Isotopic Fractionations in the Products of Vegetation Burns: Laboratory Studies. *Chem. Geol.* **1998**, *152*, 181−192.
(50) Chen, X.; Kang, S.; Cong, Z.; Yang, J.; Ma, Y. Concentration, Temporal Variation, and Sources of Black Carbon in the Mt. Everest Region Retrieved by Real-Time Observation and Simulation. *Atmos. Chem. Phys.* **2018**, *18*, 12859−12875.
(51) Lee, K.; Hur, S.; Do; Hou, S.; Burn-Nunes, L. J.; Hong, S.; Barbante, C.; Boutron, C. F.; Rosman, K. J. R. Isotopic Signatures for Natural versus Anthropogenic Pb in High-Altitude Mt. Everest Ice Cores during the Past 800years. *Sci. Total Environ.* **2011**, *412*−*413*, 194−202.
(52) Brun, F.; Berthier, E.; Wagnon, P.; Kääb, A.; Treichler, D. A Spatially Resolved Estimate of High Mountain Asia Glacier Mass Balances from 2000 to 2016. *Nat. Geosci.* **2017**, *10*, 668−673.
(53) Azam, M. F.; Ramanathan, A. L.; Wagnon, P.; Vincent, C.; Linda, A.; Berthier, E.; Sharma, P.; Mandal, A.; Angchuk, T.; Singh, V. B.; Pottakkal, J. G. Meteorological Conditions, Seasonal and Annual Mass Balances of Chhota Shigri Glacier, Western Himalaya, India. *Ann. Glaciol.* **2016**, *57*, 328−338.
(54) Kumar, A.; Attri, A. K. Biomass Combustion a Dominant Source of Carbonaceous Aerosols in the Ambient Environment of Western Himalayas. *Aerosol Air Qual. Res.* **2016**, *16*, 519−529.
(55) Saxena, M.; Sharma, S. K.; Tomar, N.; Ghayas, H.; Sen, A.; Garhwal, R. S.; Gupta, N. C.; Mandal, T. K. Residential Biomass Burning Emissions over Northwestern Himalayan Region of India: Chemical Characterization and Budget Estimation. *Aerosol Air Qual. Res.* **2016**, *16*, 504−518.
(56) Li, C.; Kang, S.; Yan, F. Importance of Local Black Carbon Emissions to the Fate of Glaciers of the Third Pole. *Environ. Sci. Technol.* **2018**, *52*, 14027−14028.
(57) Streets, D. G.; Bond, T. C.; Lee, T.; Jang, C. On the Future of Carbonaceous Aerosol Emissions. *J. Geophys. Res., D: Atmos.* **2004**, *109*, 1−19.
(58) Lamb, A. L.; Wilson, G. P.; Leng, M. J. A Review of Coastal Palaeoclimate and Relative Sea-Level Reconstructions Using Δ13C and C/N Ratios in Organic Material. *Earth-Sci. Rev.* **2006**, *75*, 29−57.
(59) Havig, J. R.; Hamilton, T. L. Snow Algae Drive Productivity and Weathering at Volcanic Rock-Hosted Glaciers. *Geochim. Cosmochim. Acta* **2019**, *247*, 220−242.
(60) Leu, E.; Wiktor, J.; Søreide, J. E.; Berge, J.; Falk-Petersen, S. Increased Irradiance Reduces Food Quality of Sea Ice Algae. *Mar. Ecol. Prog. Ser.* **2010**, *411*, 49−60.
(61) Rabha, S.; Saikia, J.; Subramanyam, K. S. V.; Hower, J. C.; Hood, M. M.; Khare, P.; Saikia, B. K. Geochemistry and Nanomineralogy of Feed Coals and Their Coal Combustion Residues from Two Different Coal-Based Industries in Northeast India. *Energy Fuels* **2018**, *32*, 3697−3708.
(62) Yang, W. *High Precision Determination of Trace Elements in Crude Oils by Using Inductively Coupled Plasma Optical Emission Spectrometry and Inductively Coupled Plasma-Mass Spectrometry*; University of Houston, 2014. https://doi.org/http://hdl.handle.net/10657/1615.
(63) Clift, P. D.; Lee, J. I.; Hildebrand, P.; Shimizu, N.; Layne, G. D.; Blusztajn, J.; Blum, J. D.; Garzanti, E.; Ali, A. Nd and Pb Isotope Variability in the Indus River System: Implications for Sediment Provenance and Crustal Heterogeneity in the Western Himalaya. *Earth Planet. Sci. Lett.* **2002**, *200*, 91−106.
(64) Ghosh, N.; Basu, A. R.; Bhargava, O. N.; Shukla, U. K.; Ghatak, A.; Garzione, C. N.; Ahluwalia, A. D. Catastrophic Environmental Transition at the Permian-Triassic Neo-Tethyan Margin of Gondwanaland: Geochemical, Isotopic and Sedimentological Evidence in the Spiti Valley, India. *Gondwana Res.* **2016**, *34*, 324−345.
(65) Deb, M.; Thorpe, R. I.; Cumming, G. L.; Wagner, P. A. Age, Source and Stratigraphic Implications of Pb Isotope Data for Conformable, Sediment-Hosted, Base Metal Deposits in the Proterozoic Aravalli-Delhi Orogenic Belt, Northwestern India. *Precambrian Res.* **1989**, *43*, 1−22.
(66) Gelly, R.; Fekiacova, Z.; Guihou, A.; Doelsch, E.; Deschamps, P.; Keller, C. Lead, Zinc, and Copper Redistributions in Soils along a Deposition Gradient from Emissions of a Pb-Ag Smelter Decommissioned 100 years Ago. *Sci. Total Environ.* **2019**, *665*, 502−512.
(67) Gariépy, C.; Allègre, C. J.; Rong Hua, Xu. The Pb-Isotope Geochemistry of Granitoids from the Himalaya-Tibet Collision Zone: Implications for Crustal Evolution. *Earth Planet. Sci. Lett.* **1985**, *74*, 220−234.
(68) Das, R.; Bin Mohamed Mohtar, A. T.; Rakshit, D.; Shome, D.; Wang, X. Sources of Atmospheric Lead (Pb) in and around an Indian Megacity. *Atmos. Environ.* **2018**, *193*, 57−65.

https://dx.doi.org/10.1021/acs.est.0c02710
Environ. Sci. Technol. 2020, 54, 8612−8621

(69) Wang, Z.; Dwyer, G. S.; Coleman, D. S.; Vengosh, A. Lead Isotopes as a New Tracer for Detecting Coal Fly Ash in the Environment. *Environ. Sci. Technol. Lett.* **2019**, *6*, 714−719.
(70) Kumar, S.; Aggarwal, S. G.; Sarangi, B.; Malherbe, J.; Barre, J. P. G.; Berail, S.; Séby, F.; Donard, O. F. X. Understanding the Influence of Open-Waste Burning on Urban Aerosols Using Metal Tracers and Lead Isotopic Composition. *Aerosol Air Qual. Res.* **2018**, *18*, 2433−2446.
(71) Kumar, S.; Aggarwal, S. G.; Malherbe, J.; Barre, J. P. G.; Berail, S.; Gupta, P. K.; Donard, O. F. X. Tracing Dust Transport from Middle-East over Delhi in March 2012 Using Metal and Lead Isotope Composition. *Atmos. Environ.* **2016**, *132*, 179−187.
(72) Sen, I. S.; Bizimis, M.; Tripathi, S. N.; Paul, D. Lead Isotopic Fingerprinting of Aerosols to Characterize the Sources of Atmospheric Lead in an Industrial City of India. *Atmos. Environ.* **2016**, *129*, 27−33.
(73) Bollhöfer, A.; Rosman, K. J. R. The Temporal Stability in Lead Isotopic Signatures at Selected Sites in the Southern and Northern Hemispheres. *Geochim. Cosmochim. Acta* **2002**, *66*, 1375−1386.
(74) Abouchami, W.; Näthe, K.; Kumar, A.; Galer, S. J. G.; Jochum, K. P.; Williams, E.; Horbe, A. M. C.; Rosa, J. W. C.; Balsam, W.; Adams, D.; Mezger, K.; Andreae, M. O. Geochemical and Isotopic Characterization of the Bodélé Depression Dust Source and Implications for Transatlantic Dust Transport to the Amazon Basin. *Earth Planet. Sci. Lett.* **2013**, *380*, 112−123.
(75) Sun, S. S. Lead Isotopic Studty of Young Volcanic Rocks from Mid-Ocean Ridges, Ocean Islands and Islands Arcs. *Philos. Trans. R. Soc., A* **1980**, *297*, 409−445.
(76) Rousseau, D. D.; Chauvel, C.; Sima, A.; Hatté, C.; Lagroix, F.; Antoine, P.; Balkanski, Y.; Fuchs, M.; Mellett, C.; Kageyama, M.; Ramstein, G.; Lang, A. European Glacial Dust Deposits: Geochemical Constraints on Atmospheric Dust Cycle Modeling. *Geophys. Res. Lett.* **2014**, *41*, 7666−7674.
(77) Ferrat, M.; Weiss, D. J.; Dong, S.; Large, D. J.; Spiro, B.; Sun, Y.; Gallagher, K. Lead Atmospheric Deposition Rates and Isotopic Trends in Asian Dust during the Last 9.5kyr Recorded in an Ombrotrophic Peat Bog on the Eastern Qinghai-Tibetan Plateau. *Geochim. Cosmochim. Acta* **2012**, *82*, 4−22.
(78) Bory, A. J. M.; Abouchami, W.; Galer, S. J. G.; Svensson, A.; Christensen, J. N.; Biscaye, P. E. A Chinese Imprint in Insoluble Pollutants Recently Deposited in Central Greenland as Indicated by Lead Isotopes. *Environ. Sci. Technol.* **2014**, *48*, 1451−1457.
(79) Biscaye, P. E.; Grousset, F. E.; Revel, M.; Gaast, S. V. D.; Zielinski, G. A.; Vaars, A.; Kukla, G. Asian Provenance of Glacial Dust (Stage 2) in the GISP2 Ice Core, Summit, Greenland. *J. Geophys. Res.* **1997**, *102*, 26315−26886.
(80) Kurkjian, R.; Dunlap, C.; Flegal, A. R. Lead Isotope Tracking of Atmospheric Response to Post-Industrial Conditions in Yerevan, Armenia. *Atmos. Environ.* **2002**, *36*, 1421−1429.
(81) Hansmann, W.; Koppel, V. Lead-Isotopes as Tracers of Pollutants in Soils. *Chem. Geol.* **2000**, *171*, 123−144.
(82) Chow, T. J.; Johnstone, M. S. Lead Isotopes in Gasoline and Aerosols of Los Angeles Basin, California. *Science* **1965**, *147*, 502−503.
(83) Monna, F.; Lancelot, J.; Croudace, I. W.; Cundy, A. B.; Lewis, J. Pb Isotopic Composition of Airborne Particulate Material from France and the Southern United Kingdom: Implications for Pb Pollution Sources in Urban Areas. *Environ. Sci. Technol.* **1997**, *31*, 2277−2286.
(84) Sangster, D. F.; Outridge, P. M.; Davis, W. J. Stable Lead Isotope Characteristics of Lead Ore Deposits of Environmental Significance. *Environ. Rev.* **2002**, *8*, 115−147.

https://dx.doi.org/10.1021/acs.est.0c02710
Environ. Sci. Technol. 2020, 54, 8612−8621